Author Contributions:
Conceptualization: Madeleine K. Youngs, Nicole S. Lovenduski
Formal analysis: Madeleine K. Youngs, Mara A. Freilich
Investigation: Madeleine K. Youngs
Methodology: Madeleine K. Youngs, Mara A. Freilich
Supervision: Nicole S. Lovenduski
Visualization: Madeleine K. Youngs, Mara A. Freilich
Writing – original draft: Madeleine K. Youngs, Mara A. Freilich
Writing – review & editing: Madeleine K. Youngs, Mara A. Freilich, Nicole S. Lovenduski

Air-Sea CO_2 Fluxes Localized by Topography in a Southern Ocean Channel

Madeleine K. Youngs[1] , **Mara A. Freilich[2,3]** , **and Nicole S. Lovenduski[4]**

[1]Atmospheric and Oceanic Sciences, University of California Los Angeles, Los Angeles, CA, USA, [2]Scripps Institution of Oceanography, University of California San Diego, La Jolla, CA, USA, [3]Now at Division of Applied Mathematics, Department of Earth, Environmental, and Planetary Sciences, Brown University, Providence, RI, USA, [4]Department of Atmospheric and Oceanic Sciences and Institute of Arctic and Alpine Research, University of Colorado Boulder, Boulder, CO, USA

Abstract Air-sea exchange of carbon dioxide (CO_2) in the Southern Ocean plays an important role in the global carbon budget. Previous studies have suggested that flow around topographic features of the Southern Ocean enhances the upward supply of carbon from the deep to the surface, influencing air-sea CO_2 exchange. Here, we investigate the role of seafloor topography on the transport of carbon and associated air-sea CO_2 flux in an idealized channel model. We find elevated CO_2 outgassing upstream of a seafloor ridge, driven by anomalous advection of dissolved inorganic carbon. Argo-like Lagrangian particles in our channel model sample heterogeneously in the vicinity of the seafloor ridge, which could impact float-based estimates of CO_2 flux.

Plain Language Summary The Southern Ocean, the ocean surrounding Antarctica, contributes significantly to carbon exchange between the global ocean and the atmosphere, which in turn matters for climate change. Here, we use a simplified model of the Southern Ocean to see how mountain ranges on the sea floor influence the carbon exchange at the ocean-atmosphere interface. We find that the seafloor mountain ranges lead to more carbon exchange. Floating carbon sensors in our model ocean may under or over sample the water near the mountains and this can affect the carbon exchange that they report.

1. Introduction

The Southern Ocean is an active driver in the global cycling of carbon dioxide (CO_2). Studies based on coarse-resolution ocean general circulation models suggest that the Southern Ocean carbon cycle is characterized by the surfacing of old, respired carbon from depth at high latitudes and the subduction of anthropogenic carbon driven by the meridional overturning circulation from the surface into the interior at mid latitudes (Mikaloff Fletcher et al., 2006, 2007). Similarly, Chen et al. (2022) connect the surface dissolved inorganic carbon to interior pathways (i.e., overturning) of the dissolved inorganic carbon using observations. However, observations of the resulting air-sea CO_2 fluxes from these physical circulation processes are sparse in both space and time (Bakker et al., 2016), and this has limited our ability to accurately quantify the Southern Ocean's role in the global carbon budget. New observations from autonomous floats equipped with pH sensors as part of the Southern Ocean Carbon and Climate Observations and Modeling (SOCCOM) program suggest that the outgassing of respired carbon in high latitudes has previously been underestimated (Bushinsky et al., 2019; Gray et al., 2018), in disagreement with satellite-derived CO_2 outgassing (Long et al., 2021), suggesting there is more work to be done to constrain the air-sea carbon fluxes.

One contributing factor to the uncertainty in the Southern Ocean carbon budget is spatial variability in the air-sea CO_2 flux that is engendered by regional variations in the physical circulation. While the canonical view of Southern Ocean circulation is an annular circumpolar current with a broad region of surface divergence and upwelling at ~55°S and convergence and subduction at ~40°S (Speer et al., 2000), current literature highlights the non-annular nature of the circumpolar current (Rintoul, 2018) and associated overturning circulation (Youngs & Flierl, 2023). Seafloor topographic features such as ridges create standing meanders in the current and drive localized upwelling (e.g., Tamsitt et al., 2017; Youngs & Flierl, 2023), and it is thought that these topographic features may play an important role in carbon fluxes and tracer transports (Balwada et al., 2018). High resolution ocean circulation and biogeochemical modeling studies suggest that standing meanders contribute to southward

transport of anthropogenic carbon (Ito et al., 2010), and that intensified residual upwelling downstream of regional topographic features provides an important conduit for deep, natural carbon to enter the Southern Ocean surface (Brady et al., 2021). Despite the potentially important role that these regional topographic features play in the global carbon budget, no study has directly quantified the influence of seafloor topography on Southern Ocean air-sea CO_2 flux nor addressed the potential effects these features may have on Lagrangian observations of the Southern Ocean.

Here, we use an idealized, high-resolution ocean general circulation and biogeochemical model to assess the role of seafloor topography in Southern Ocean air-sea CO_2 fluxes and the ability to quantify these fluxes via Lagrangian observations. Our study demonstrates that seafloor topography has a substantial impact on local CO_2 flux via topography-driven advection of dissolved inorganic carbon (DIC). Lagrangian particles tend to heterogeneously sample the surface pCO_2 in the vicinity of topography, and this can affect estimates of average air-sea CO_2 fluxes over the region. In Section 2, we present the methods used, in Section 3 we present the results. In Section 4 we discuss and conclude.

2. Methods

2.1. Model Description

For this study, we use an idealized-geometry MITgcm ocean channel model (Youngs & Flierl, 2023) and couple it to a simple ocean biogeochemical model (Dutkiewicz et al., 2005; Lauderdale et al., 2016). The channel is 4,000 km long and 2,000 km wide with 10 km horizontal resolution (Figure 1) with a total depth of 4,000 m with 32 vertical levels, from 10 m vertical grid spacing at the surface to 280 m at the bottom. We represent seafloor topography using a 2,000 m tall Gaussian ridge with a 200 km half-width, centered 800 km downstream of the channel entrance spanning the channel north to south (Figure 1). The domain is periodic with the outflow in the east reentering in the western boundary and free-slip walls at the north and the south. The model is integrated using a 600 s time step, an exponentially varying diffusivity (0.01 m^2 s^{-1} decreasing downward to 1×10^{-5} m^2 s^{-1}), and linear bottom drag with a drag coefficient of 1.1×10^{-3} m s^{-1}. The wind stress is a cosine profile with a maximum value of 0.15 N m^{-2} at the center of the domain and zero wind stress at the sides (Figure S1 in Supporting Information S1). The salinity is set at 35 PSU and not allowed to vary.

We employ the DIC package from MITgcm to represent biogeochemistry in our model (Dutkiewicz et al., 2005; Lauderdale et al., 2016). This model package carries alkalinity, DIC, dissolved organic phosphate, and phosphate as biogeochemical tracers, and represents biological uptake as a function of phosphate and light availability. Phosphate is fluxed vertically with remineralization and sinking (see more in the SI). The calcium carbonate formation is proportional to the organic phosphorous produced in the surface waters following the parameterization of Yamanaka and Tajika (1996), with sinking and dissolution (Dutkiewicz et al., 2005).

The rate of change of carbon in our model can be described by the following equation (Lauderdale et al., 2016)

$$\frac{\partial C_T}{\partial t} = \underbrace{-\nabla \cdot \left(\vec{u}C_T\right)}_{\text{Advection}} + \underbrace{\nabla \cdot (\kappa \nabla C_T)}_{\text{Diffusion}} \underbrace{-R_{C_T:P}S_{bio} - S_{CaCO_3}}_{\text{Biology}} \underbrace{-\frac{F_{CO_2}}{h}}_{\text{Air-sea fluxes}} , \qquad (1)$$

where C_T is the concentration of total dissolved organic carbon, κ is the eddy diffusivity tensor, $R_{C_T:P}$ is the biological transformation between carbon and phosphorous and F_{CO_2} is the air-sea CO_2 flux, h is the mixed layer depth, S_{bio} represents the sources and sinks of biogenic soft tissue, and S_{CaCO_3} represents the sources and sinks of biogenic carbonate. Note that this equation neglects the dilution by freshwater fluxes, which in our case is appropriate due to a lack of salinity or freshwater forcing.

The model is initialized with a uniform surface ocean pCO_2 of 270 ppm with DIC and alkalinity at the northern boundary sponge region relaxed to prescribed preindustrial DIC and alkalinity profiles based on GLODAPv2.2016 (Key et al., 2015; Lauvset et al., 2016) (Figure S3 in Supporting Information S1), and spun up for 30 years for the biogeochemical and physical tracers to reach an approximate steady-state (Table S1 in Supporting Information S1). At the end of the spin-up period, our model simulates similar Southern Ocean-integrated pre-industrial air-sea CO_2 fluxes (0.1 mol m^{-2} yr^{-1}) as those estimated from more realistic model configurations (0.13 mol m^{-2} yr^{-1}) (e.g., Lovenduski et al., 2007). The atmospheric CO_2 is held at a preindustrial value of 270 ppm and the air sea fluxes are calculated via a bulk formula.
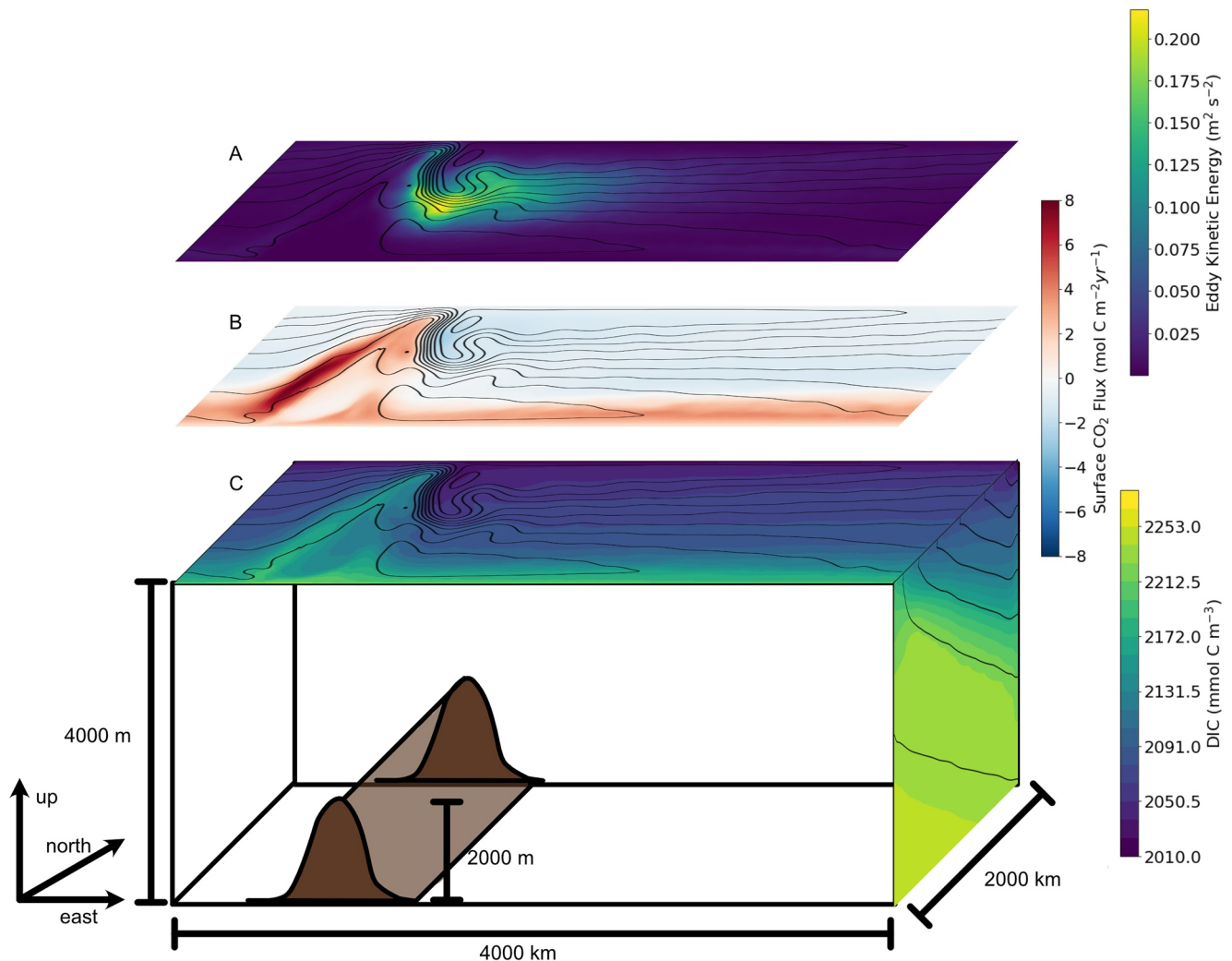
Figure 1. The model is a re-entrant channel forced with both a zonal wind and a relaxation to a meridional temperature gradient. Barotropic streamlines are shown with black contours on the top faces. Shading shows temporally-averaged (a) surface eddy kinetic energy, (b) surface carbon dioxide flux, and (c) dissolved inorganic carbon (DIC) concentration. In (c) the right edge shows temporally and zonally averaged DIC concentration with temperature (density) contoured in black. The model geometry is shown in (c). A 2000 m tall undersea Gaussian ridge is centered at $x = 800$ km.

2.2. Particle Tracking

We model idealized "Argo" float trajectories to estimate how well a biogeochemical Argo float array can sample the air-sea carbon fluxes as a function of float density. We use the Ocean Parcels package to track idealized Argo floats (https://oceanparcels.org/) (Lange & van Sebille, 2017). We release 800 floats spaced uniformly throughout the model domain. Real Argo floats park at 1,000 m depth for 10 days between profiles, so in our simulations the particles are advected using daily-averaged velocities at 1,000 m; they sample the surface ocean pCO_2 at their position every 10 days. Idealized (and real) Argo floats are advected in a 2D velocity field, which could be convergent/divergent because they cannot follow the vertical flow. Idealized floats are advected for 1 or 3 years. We run four collections of experiments: 10 floats for 1 year, 33 floats for 1 year, 100 floats for 1 year, and 33 floats for 3 years. For each collection, we select 100 instances of that number of floats (from a larger collection of 800 floats) for the time series in question to calculate statistics. We use the randomly subsampled float data to create a climatology using objective mapping (e.g., Figure 3b). From the mapped pCO_2, we calculate the air-sea carbon fluxes using the same equations used by the model (Wanninkhof, 1992).

Objective mapping is a commonly used and well-justified technique for mapping sparsely sampled data to estimate regional averages (Dong et al., 2008; Friedrich & Oschlies, 2009; Reeve et al., 2016). We
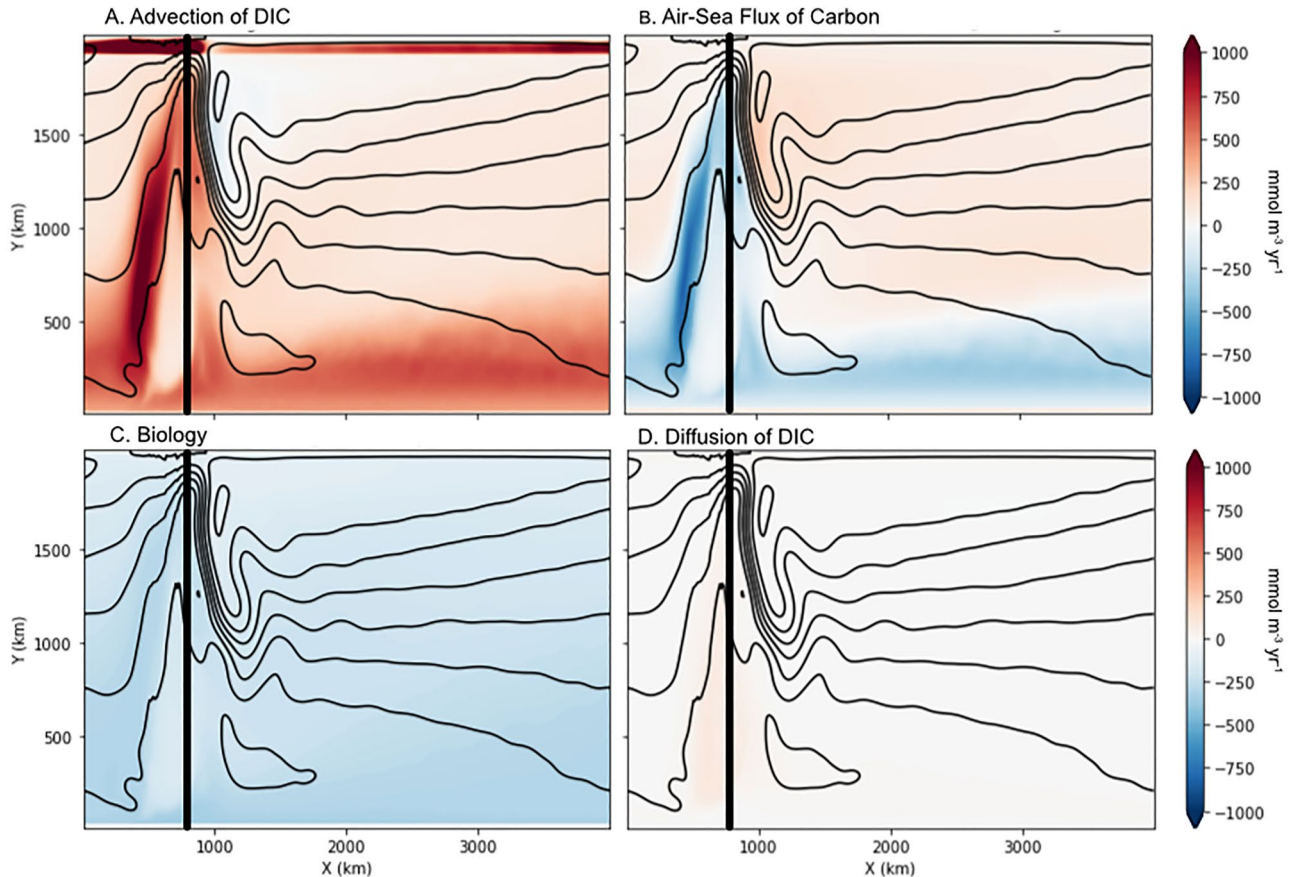
Figure 2. The drivers of the rate of change of DIC ($\frac{\partial C_T}{\partial t}$; mmol m^{-3} yr^{-1}), as in Equation 1, averaged over the 20 years simulation and the top 50 m: (a) DIC advection, (b) sea-air flux of CO$_2$, (c) biology, and (d) DIC diffusion. The vertical lines indicate the location of the top of the ridge.

create climatologies of these samples using the ordinary kriging method with the PyKrige Python package (https://github.com/GeoStat-Framework/PyKrige/). Here, the various terms for the Gaussian variogram are fit using the data from the selected floats to create the most optimal map.

3. Results

3.1. DIC Budget

We investigate the asymmetry of the carbon properties in the channel model. Both air-sea CO$_2$ flux and surface DIC concentration exhibit large zonal asymmetry, with enhanced CO$_2$ outgassing and elevated surface DIC located just upstream of the undersea ridge (Figures 1b and 1c). Away from the influence of topography, our model exhibits moderate outgassing of CO$_2$ near the southern boundary, with weak uptake in the northern part of the domain (Figure 1b), which together contribute to an average flux of about -0.07 mol C m^{-2} yr^{-1}. At the latitudes of the topographic ridge, however, we find sea-air CO$_2$ fluxes that exceed 7 mol C m^{-2} yr^{-1} and outgassing that extends to the northern boundary of the domain, with an average flux of 0.8 mol C m^{-2} yr^{-1}. The enhanced carbon flux is located in the region where the barotropic flow turns north as it approaches the ridge (Figures 1b and 1c). This region is characterized by elevated surface DIC concentrations relative to the zonal mean for the domain (Figure 1c). We also show that as the wind stress forcing changes, the pCO$_2$ flux changes are driven by changes in advection of DIC not other terms like temperature forcing or changes in alkalinity (Figure S5 in Supporting Information S1), highlighting the importance of the advection of DIC.

We investigate the drivers of the elevated surface ocean DIC upstream of the topographic ridge by quantifying the terms in Equation 1 averaged over the top 50 m. DIC advection tends to increase DIC upstream of the ridge, while sea-air CO$_2$ flux tends to decrease DIC in this same region (Figures 2a and 2b). In contrast, biological
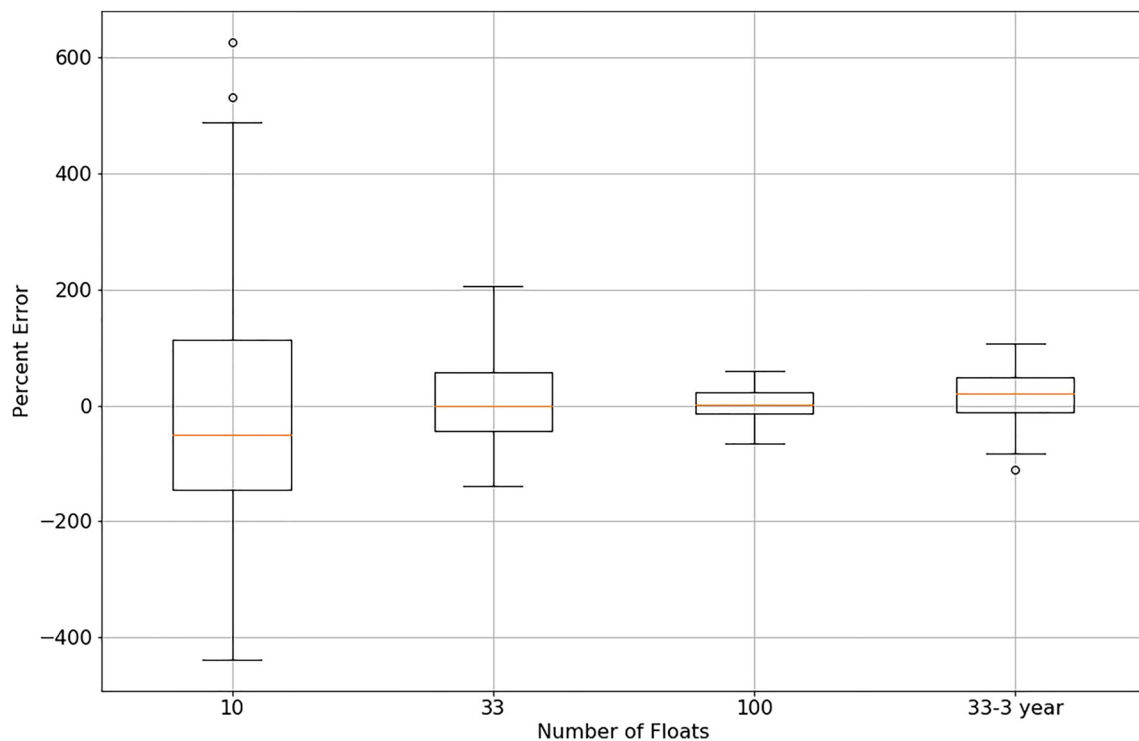
Figure 3. Percent error in the domain-integrated sea-air CO_2 fluxes with Argo-like model sampling for 10, 33, and 100 floats advected for one year and 33 floats advected for 3 years, respectively. The results of 100 trials with randomly initialized floats are shown for each float density. The boxes show the interquartile range and median (orange line) and the whiskers show 1.5 times the interquartile range over the 100 trials. Positive numbers represent anomalous CO_2 outgassing in the float estimate.

productivity tends to decrease DIC relatively uniformly over the domain, with only a slightly larger influence upstream of the ridge, and DIC diffusion exhibits only a small influence on upper ocean DIC tendency across the domain (Figures 2c and 2d). The elevated net DIC advection upstream of the ridge is mostly driven by vertical advection (Figure S4 in Supporting Information S1), though the contribution from the horizontal advection of DIC is non-negligible, especially in the northern portion of the model domain (Figure S4 in Supporting Information S1). Thus, results from our DIC tendency budget suggest that enhanced vertical advection of DIC upstream of the ridge is responsible for the locally elevated DIC, and by inference, the enhanced outgassing of CO_2 in this region. Our model also simulates elevated sea-air CO_2 flux and surface ocean DIC in the northern portion of model domain over the ridge, albeit with lower magnitudes than in the region upstream of the ridge (Figure 1). Here, the elevated DIC is driven by DIC advection (Figure 2), with horizontal DIC advection playing a key role (Figure S4 in Supporting Information S1).

3.2. Sampling Heterogeneous Carbon Fluxes

Topography-induced heterogeneity may challenge observation of ocean carbon processes. We quantify the ability of autonomous, Lagrangian floats to sample surface ocean DIC and associated CO_2 fluxes by adding idealized particles to our model domain. We test four deployment strategies (a) 10 floats for one year, (b) 33 floats for one year, (c) 100 floats for one year, and (d) 33 floats for 3 years. For each float number and duration we select 100 collections of random initial conditions. We calculate the error by subtracting the model truth from the calculated air-sea CO_2 fluxes, integrating over the residual and normalizing by the integrated value of the model truth air-sea CO_2 fluxes. As such, our error estimate is fairly conservative; the error would certainly be larger using a square error metric.

Our idealized sampling approach reveals substantial biases in the domain-integrated CO_2 flux, as compared to the model truth. With 10 floats, the interquartile range of the air-sea CO_2 flux error is large, from a 113% over-estimate to a −146% underestimate, with larger extremes in the upper and lower 25% of the realizations. In this

case, the median error (median = −50%, mean = −11%) is an underestimate of the net fluxes. With 33 floats over 1 year the interquartile range is smaller but still quite large—a 57% overestimate to a −45% underestimate (with mean = 2% and median = −1%). With 100 random floats, the error is substantially smaller with an interquartile range of −13%–23%, and the median (1%) and mean (3%) indicate an overestimate of the carbon flux. When we advect 33 floats for 3 years, the error is larger than 100 floats for a single year, with an interquartile range of −11%–48% and a positive flux bias (mean = 18%, median = 20%). Our analysis reveals that the interquartile range of the error of air-sea CO_2 fluxes is quite large when we simulate a float density comparable to the current SOCCOM array (33 floats in a 4,000 km sector of the Southern Ocean). Both adding more floats and advecting the floats for 3 years reduces the error. However, even in the absence of interannual variability, 33 floats advected for 3 years has an increased error range and a positive bias when compared with 100 floats for 1 year.

The bias in the idealized float-like sampling of surface carbon arises from the influence of topography on the float trajectories (Figure 4), which results in two factors that influence statistical estimation of air-sea fluxes from Lagrangian trajectories. First, the highly skewed distribution of air-sea fluxes means that bias can be present with low sample numbers before the sample means converge to a normal distribution (as predicted by the Central Limit Theorem). As an example of the influence of topographically influenced sampling on the calculated air-sea CO_2 fluxes, we show annual-mean fluxes derived from the model (Figure 4a), calculated using the mapped pCO_2 as sampled by 33 floats (Figure 4b; float trajectories in black), and the difference between the model truth and the subsampled fluxes, where blue indicates an underestimate by the floats and red is an overestimate (Figure 4c). In this example, the floats produce a large underestimate of flux upstream of the ridge due to a lack of sampling in this region (Figure 4c). However, the CO_2 flux is overestimated in other regions (Figure 4c), such the net error is an overestimate of 19%. The full statistical distribution is shown in Figure S11 in Supporting Information S1. Second, Lagrangian particles do not uniformly sample the Eulerian distribution of air-sea fluxes (Figure S10 in Supporting Information S1). Sample statistics are drawn from the Lagrangian rather than Eulerian distribution. Particles tend to follow barotropic streamlines as they circumnavigate the Southern Ocean in our model (e.g., Figure 4b). Ahead of the ridge, particles either slow down or speed up (Figure S9 in Supporting Information S1), with the long residence times where the air-sea carbon fluxes are the largest, which combined with widely spaced streamlines (Figure 4) indicates that the particles tend to avoid this region when not directly seeded in this region. Because of this, despite the random initial particle seeding, we hypothesize that sparsely populated particles tend to undersample the region upstream of topography which particles tend to avoid (e.g., Figure 4b) and oversample the region downstream of topography (e.g., Figure 4b) where eddy kinetic energy is at a maximum (Figure 1a).

4. Conclusions and Discussion

Using an idealized channel model of the Southern Ocean with an undersea ridge, we examine the influence of topography on air-sea CO_2 fluxes. We find intense sea-air CO_2 fluxes and elevated surface ocean DIC upstream of topography, driven by enhanced DIC advection. Due to the nature of the flow near topography, relatively sparse Argo-like particles in our model tend to undersample the region upstream of the ridge and oversample the region downstream of the ridge, leading to biases in domain-integrated CO_2 fluxes.

In a previous paper using the same idealized model, Youngs and Flierl (2023) find localized upwelling upstream of the topographic ridge in association with a standing eddy; this localized upwelling is collocated with the region of enhanced CO_2 outgassing reported in this study, suggesting that the standing eddy induced by topography can affect air-sea CO_2 exchange. As water parcels approach the ridge, the flow is deflected northward, which also steepens the isopycnal surfaces and produces a vertical flux of DIC consistent with the along-isopycnal vertical tracer flux mechanism described in Freilich and Mahadevan (2019). Biogeochemical tracers, such as DIC in this case, have gradients along isopycnal surfaces and stirring across those gradients leads to a net flux. Relaxation of the inclined isopycnal surface in response to semigeostrophic frontogenesis results in an ageostrophic circulation with net upward flux on the light side of the front (east of the ridge on the upstream side) that is inclined relative to the isopycnal surface (Hoskins, 1982).

The largest outgassing is associated with the barotropic effect of topographic features. Lagrangian floats advected at 1,000 m are influenced by this topographic effect. Our results show that Lagrangian particle density is highest in regions with the highest EKE, consistent with the study of Wang et al. (2020). Yet, our model predicts that the region associated with the highest DIC and thus the largest sea-air CO_2 flux occurs upstream of the ridge, in a region with large gradients in barotropic flow and DIC that tends to be undersampled by Lagrangian particles.
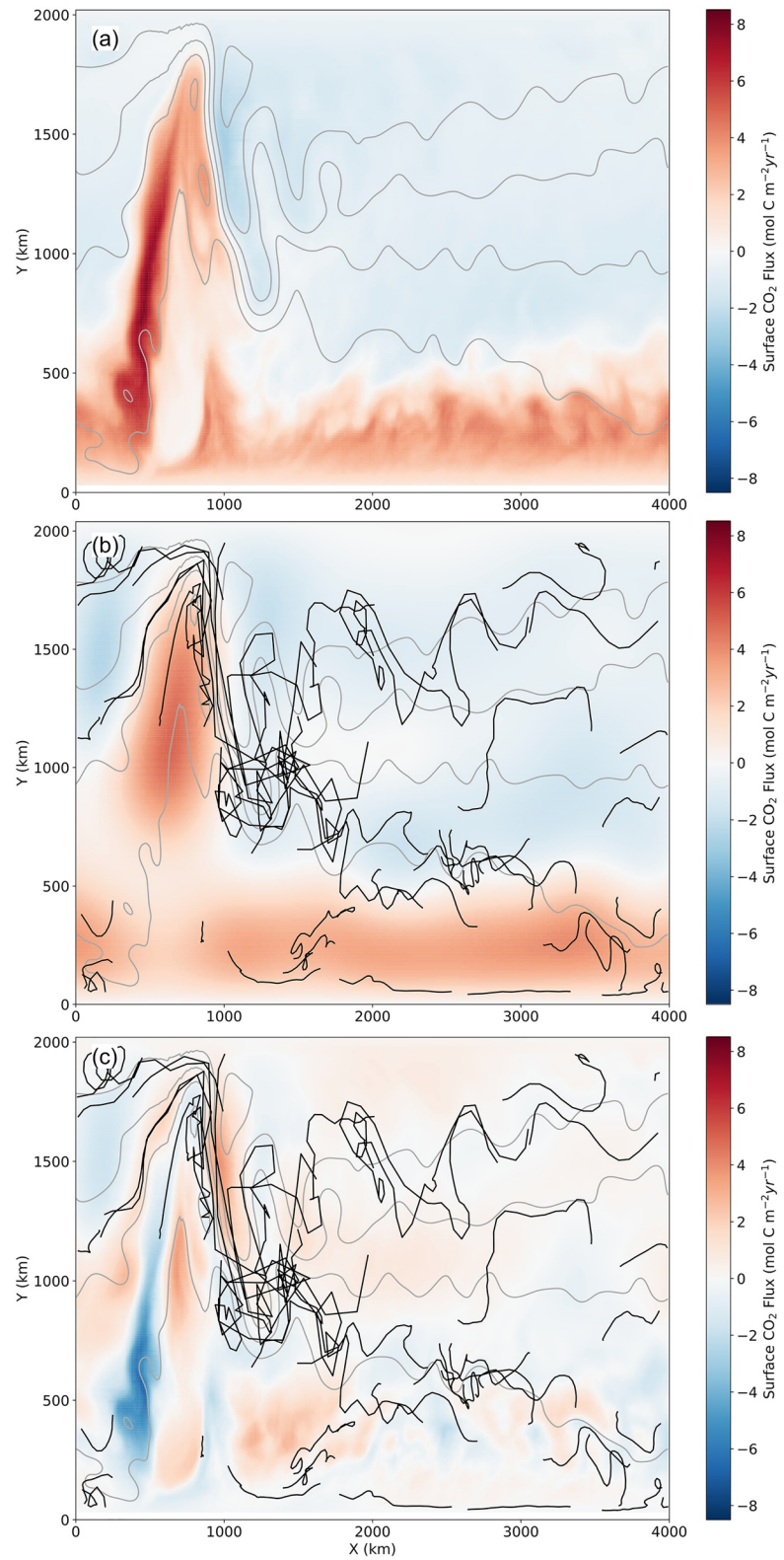
Figure 4. Air-sea CO_2 fluxes over one year derived from the idealized channel model. (a) Modeled fluxes, (b) fluxes as sampled by 33 randomly spaced particles, and (c) the difference between the sub-sampled fluxes and the model truth, with a 19% overestimate of the fluxes. Gray contours indicate barotropic streamlines, while black lines show the tracks of the 33 floats used to generate the images in panels (b) and (c).

While previous studies have identified topographic upwelling and outgassing of CO_2, most have suggested that this effect is due to the high eddy kinetic energy downstream of topographic features (Barthel et al., 2022; Brady et al., 2021; Dufour et al., 2015; Tamsitt et al., 2017; Viglione & Thompson, 2016; Yung et al., 2022). Here, by using an idealized process study, we have identified the standing eddy upstream of topography as the dominant cause of upwelling. Future work should test the sensitivity of this result to more complex topography, more realistic atmospheric forcing, and model resolution. This particular mechanism, driven by a standing eddy projection upstream of the domain, may be somewhat reproducible without resolving mesoscale eddies, however, the eddies are necessary for maintaining appropriate gradients.

Our findings suggest that Lagrangian floats may undersample topographically induced biogeochemical anomalies (e.g., DIC, oxygen, nitrate). Future efforts in observational network design should consider alternate methods to estimate the biogeochemistry of topographically influenced regions. One approach is to use alternative technologies such as gliders (e.g., Dove et al., 2021). This study uses the current standard Gaussian objective mapping technique to map surface ocean pCO_2 and infer air-sea CO_2 fluxes. A complementary approach to confronting the challenges posed by Lagrangian autonomous sampling platforms is developing mapping techniques that account for heterogeneous environments such as techniques that utilize information about correlation length scales (Chamberlain, 2022), and those that use ancillary data such as temperature and salinity to map biogeochemical variables (A. Gray, pers. comm.). Such approaches may improve the sampling error in topographically influenced regions.

The idealized model geometry used in this study has enabled mechanistic insights into the drivers of outgassing hotspots at topographic features in the Southern Ocean (Brady et al., 2021; Tamsitt et al., 2017). The insight that barotropic effects have a primary role in driving outgassing hotspots has direct implications for observing system design. Increasing model complexity through more complex and realistic model geometry, improved realism of multiple biogeochemical tracers, finer resolution model configurations, and seasonal variability that can improve representation of wind-current interactions (Kwak et al., 2021) may enable additional insights about the ways that zonal asymmetry influences the Southern Ocean carbon cycle and the coupling between DIC and other biogeochemical factors in the Southern Ocean.

Seafloor topography induces anomalies in both the flow and the surface ocean DIC concentration, leading to sub-optimal sampling of a key region for Southern Ocean CO_2 flux. Through the mechanistic insight provided by this study, we suggest that the current SOCCOM float array has most likely undersampled (rather than over-sampled) potential areas of CO_2 outgassing in the Southern Ocean, which could further amplify the differences in CO_2 fluxes estimated from SOCCOM floats and those estimated from ship- or satellite-based observations (Bushinsky et al., 2019; Gray et al., 2018; Long et al., 2021). Topographically influenced regions in the Southern Ocean should be a focus for future biogeochemical observation and modeling programs.

Data Availability Statement

The code used to run the model is available at https://zenodo.org/badge/latestdoi/629141314. The GLODAPv2 data is available at https://www.nodc.noaa.gov/archive/arc0107/0162565/1.1/data/0-data/mapped/GLODAPv2.2016b_MappedClimatologies.tar.gz.

References

Bakker, D. C., Pfeil, B., Landa, C. S., Metzl, N., O'brien, K. M., Olsen, A., et al. (2016). A multi-decade record of high-quality fCO$_2$ data in version 3 of the surface ocean CO$_2$ atlas (SOCAT). *Earth System Science Data*, *8*(2), 383–413.

Balwada, D., Smith, K. S., & Abernathey, R. (2018). Submesoscale vertical velocities enhance tracer subduction in an idealized Antarctic circumpolar current. *Geophysical Research Letters*, *45*(18), 9790–9802. https://doi.org/10.1029/2018gl079244

Barthel, A., Hogg, A. M., Waterman, S., & Keating, S. (2022). Baroclinic control of southern ocean eddy upwelling near topography. *Geophysical Research Letters*, *49*(7), e2021GL097491. https://doi.org/10.1029/2021gl097491

Brady, R. X., Maltrud, M. E., Wolfram, P. J., Drake, H. F., & Lovenduski, N. S. (2021). The influence of ocean topography on the upwelling of carbon in the Southern Ocean. *Geophysical Research Letters*, *48*(19), e2021GL095088. https://doi.org/10.1029/2021gl095088

Bushinsky, S. M., Landschützer, P., Rödenbeck, C., Gray, A. R., Baker, D., Mazloff, M. R., et al. (2019). Reassessing Southern Ocean air-sea CO$_2$ flux estimates with the addition of biogeochemical float observations. *Global Biogeochemical Cycles*, *33*(11), 1370–1388. https://doi.org/10.1029/2019gb006176

Chamberlain, P. M. (2022). *Semi-Lagrangian float motion and observing system design*. Ph.D. Dissertation, University of California, San Diego. Retrieved from https://escholarship.org/uc/item/2jt5p0q2

Chen, H., Haumann, F. A., Talley, L. D., Johnson, K. S., & Sarmiento, J. L. (2022). The deep ocean's carbon exhaust. *Global Biogeochemical Cycles*, *36*(7), e2021GB007156. https://doi.org/10.1029/2021gb007156

Dong, S., Sprintall, J., Gille, S. T., & Talley, L. (2008). Southern Ocean mixed-layer depth from Argo float profiles. *Journal of Geophysical Research*, *113*(C6), C06013. https://doi.org/10.1029/2006jc004051

Dove, L. A., Thompson, A. F., Balwada, D., & Gray, A. R. (2021). Observational evidence of ventilation hotspots in the Southern Ocean. *Journal of Geophysical Research: Oceans*, *126*(7), e2021JC017178. https://doi.org/10.1029/2021jc017178

Dufour, C. O., Griffies, S. M., de Souza, G. F., Frenger, I., Morrison, A. K., Palter, J. B., et al. (2015). Role of mesoscale eddies in cross-frontal transport of heat and biogeochemical tracers in the southern ocean. *Journal of Physical Oceanography*, *45*(12), 3057–3081. https://doi.org/10.1175/jpo-d-14-0240.1

Dutkiewicz, S., Sokolov, A. P., Scott, J., & Stone, P. H. (2005). *A three-dimensional ocean-sea ice-carbon cycle model and its coupling to a two-dimensional atmospheric model: Uses in climate change studies (Tech. Rep.).* MIT Joint Program on the Science and Policy of Global Change.

Freilich, M. A., & Mahadevan, A. (2019). Decomposition of vertical velocity for nutrient transport in the upper ocean. *Journal of Physical Oceanography*, *49*(6), 1561–1575. https://doi.org/10.1175/jpo-d-19-0002.1

Friedrich, T., & Oschlies, A. (2009). Basin-scale pCO_2 maps estimated from ARGO float data: A model study. *Journal of Geophysical Research*, *114*(C10), C10012. https://doi.org/10.1029/2009jc005322

Gray, A. R., Johnson, K. S., Bushinsky, S. M., Riser, S. C., Russell, J. L., Talley, L. D., et al. (2018). Autonomous biogeochemical floats detect significant carbon dioxide outgassing in the high-latitude Southern Ocean. *Geophysical Research Letters*, *45*(17), 9049–9057. https://doi.org/10.1029/2018gl078013

Hoskins, B. J. (1982). The mathematical theory of frontogenesis. *Annual Review of Fluid Mechanics*, *14*(1), 131–151. https://doi.org/10.1146/annurev.fl.14.010182.001023

Ito, T., Woloszyn, M., & Mazloff, M. (2010). Anthropogenic carbon dioxide transport in the Southern Ocean driven by Ekman flow. *Nature*, *463*(7277), 80–83. https://doi.org/10.1038/nature08687

Key, R. M., Olsen, A., van Heuven, S., Lauvset, S. K., Velo, A., Lin, X., et al. (2015). Global ocean data analysis project, version 2 (GLODAPv2). Ornl/Cdiac-162, Ndp-093.

Kwak, K., Song, H., Marshall, J., Seo, H., & McGillicuddy, D. J., Jr. (2021). Suppressed pCO_2 in the Southern Ocean due to the interaction between current and wind. *Journal of Geophysical Research: Oceans*, *126*(12), e2021JC017884. https://doi.org/10.1029/2021jc017884

Lange, M., & van Sebille, E. (2017). Parcels v0. 9: Prototyping a Lagrangian ocean analysis framework for the petascale age. *Geoscientific Model Development*, *10*(11), 4175–4186. https://doi.org/10.5194/gmd-10-4175-2017

Lauderdale, J. M., Dutkiewicz, S., Williams, R. G., & Follows, M. J. (2016). Quantifying the drivers of ocean-atmosphere CO_2 fluxes. *Global Biogeochemical Cycles*, *30*(7), 983–999. https://doi.org/10.1002/2016gb005400

Lauvset, S. K., Key, R. M., Olsen, A., Van Heuven, S., Velo, A., Lin, X., et al. (2016). A new global interior ocean mapped climatology: The 1×1 GLODAP version 2. *Earth System Science Data*, *8*(2), 325–340. https://doi.org/10.5194/essd-8-325-2016

Long, M. C., Stephens, B. B., McKain, K., Sweeney, C., Keeling, R. F., Kort, E. A., et al. (2021). Strong southern ocean carbon uptake evident in airborne observations. *Science*, *374*(6572), 1275–1280. https://doi.org/10.1126/science.abi4355

Lovenduski, N. S., Gruber, N., Doney, S. C., & Lima, I. D. (2007). Enhanced CO_2 outgassing in the Southern Ocean from a positive phase of the southern annular mode. *Global Biogeochemical Cycles*, *21*(2), GB2026. https://doi.org/10.1029/2006gb002900

Mikaloff Fletcher, S. E., Gruber, N., Jacobson, A. R., Doney, S. C., Dutkiewicz, S., Gerber, M., et al. (2006). Inverse estimates of anthropogenic CO_2 uptake, transport, and storage by the ocean. *Global Biogeochemical Cycles*, *20*(2), GB2002. https://doi.org/10.1029/2005gb002530

Mikaloff Fletcher, S. E., Gruber, N., Jacobson, A. R., Gloor, M., Doney, S., Dutkiewicz, S., et al. (2007). Inverse estimates of the oceanic sources and sinks of natural CO_2 and the implied oceanic carbon transport. *Global Biogeochemical Cycles*, *21*(1), GB1010. https://doi.org/10.1029/2006gb002751

Reeve, K., Boebel, O., Kanzow, T., Strass, V., Rohardt, G., & Fahrbach, E. (2016). A gridded data set of upper-ocean hydrographic properties in the Weddell Gyre obtained by objective mapping of Argo float measurements. *Earth System Science Data*, *8*(1), 15–40. https://doi.org/10.5194/essd-8-15-2016

Rintoul, S. R. (2018). The global influence of localized dynamics in the Southern Ocean. *Nature*, *558*(7709), 209–218. https://doi.org/10.1038/s41586-018-0182-3

Speer, K., Rintoul, S. R., & Sloyan, B. (2000). The diabatic Deacon cell. *Journal of Physical Oceanography*, *30*(12), 3212–3222. https://doi.org/10.1175/1520-0485(2000)030<3212:tddc>2.0.co;2

Tamsitt, V., Drake, H. F., Morrison, A. K., Talley, L. D., Dufour, C. O., Gray, A. R., et al. (2017). Spiraling pathways of global deep waters to the surface of the Southern Ocean. *Nature Communications*, *8*(1), 1–10. https://doi.org/10.1038/s41467-017-00197-0

Viglione, G. A., & Thompson, A. F. (2016). Lagrangian pathways of upwelling in the southern ocean. *Journal of Geophysical Research: Oceans*, *121*(8), 6295–6309. https://doi.org/10.1002/2016jc011773

Wang, T., Gille, S. T., Mazloff, M. R., Zilberman, N. V., & Du, Y. (2020). DDY-induced acceleration of Argo floats. *Journal of Geophysical Research: Oceans*, *125*(10), e2019JC016042. https://doi.org/10.1029/2019JC016042

Wanninkhof, R. (1992). Relationship between wind speed and gas exchange over the ocean. *Journal of Geophysical Research*, *97*(C5), 7373–7382. https://doi.org/10.1029/92jc00188

Yamanaka, Y., & Tajika, E. (1996). The role of the vertical fluxes of particulate organic matter and calcite in the oceanic carbon cycle: Studies using an ocean biogeochemical general circulation model. *Global Biogeochemical Cycles*, *10*(2), 361–382. https://doi.org/10.1029/96gb00634

Youngs, M. K., & Flierl, G. R. (2023). Extending residual-mean overturning theory to the topographically localized transport in the southern ocean. *Journal of Physical Oceanography*, *53*(8), 1901–1915. https://doi.org/10.1175/jpo-d-22-0217.1

Yung, C. K., Morrison, A. K., & Hogg, A. M. (2022). Topographic hotspots of southern ocean eddy upwelling. *Frontiers in Marine Science*, *9*, 855785. https://doi.org/10.3389/fmars.2022.855785